

# Cell performance distribution in a low-temperature proton exchange membrane fuel cell stack during propene contamination

Jean St-Pierre<sup>1</sup> · Maheboob B. V. Virji<sup>1</sup>

Received: 10 May 2015 / Accepted: 28 September 2015 / Published online: 5 October 2015  
© Springer Science+Business Media Dordrecht 2015

**Abstract** A 36-cell proton exchange membrane fuel cell (PEMFC) stack was contaminated with 50 ppm propene in air. Propene contamination amplified the uneven cell performance distribution along the stack length. End cells showed a larger performance change due to contamination than contiguous cells owing to a lower temperature and a larger effect of contamination at lower temperatures. The performance change of the inner cells linearly varied from cell 2 to cell 35 and was attributed to several causes including the uneven sub-saturated air flow distribution and the propene oxidation reaction involving a water molecule. The inner cells performance distribution was also credited to the uneven coolant flow distribution and a large effect of temperature on contamination. Higher cathode potentials acted as a cleaning method that minimized the contamination effect by promoting propene oxidation and led to weakly adsorbing CO<sub>2</sub>. As a consequence, higher cathode potentials also resulted in smoothing the uneven inner cells performance distribution.

**Keywords** Proton exchange membrane fuel cell · Fuel cell stack · Voltage distribution · Air stream contaminant

## List of symbols

$A_{\text{end}}$  End plate heat transfer surface (m<sup>2</sup>)  
 $A_{\text{sides}}$  Cell sides heat transfer surface (m<sup>2</sup>)

**Electronic supplementary material** The online version of this article (doi:10.1007/s10800-015-0896-y) contains supplementary material, which is available to authorized users.

✉ Jean St-Pierre  
jsp7@hawaii.edu

<sup>1</sup> Hawaii Natural Energy Institute, University of Hawaii – Manoa, Honolulu, Hawaii 96822, USA

$b$  Stack inner cells performance linear regression parameter (mV cell<sup>-1</sup>)  
 $C$  Coolant heat capacity (J kg<sup>-1</sup> K<sup>-1</sup>)  
 $C_a$  Anode capacitance (F)  
 $CPE_c$  Cathode constant phase element  
 $i$  Summation index  
 $I$  Cell current (A)  
 $j$   $\sqrt{-1}$   
 $k$  Heat transfer coefficient (W K<sup>-1</sup> m<sup>-2</sup>)  
 $\dot{m}$  Coolant flux (kg s<sup>-1</sup>)  
 $n$  Cell number or number of cells  
 $Q$  Heat produced (W)  
 $Q_{CPE}$  Cathode constant phase element coefficient (s <sup>$z_{CPE}$</sup>   $\Omega^{-1}$ )  
 $Q_{\text{end}}$  Natural convection heat loss through the end plate (W)  
 $Q_{\text{inner}}$  Inner cell heat loss (W)  
 $Q_{\text{sides}}$  Natural convection heat loss through the cell sides (W)  
 $Q_1$  or  $Q_n$  End cells heat loss (W)  
 $R_a$  Hydrogen oxidation charge transfer resistance ( $\Omega$ )  
 $R_c$  Oxygen reduction charge transfer resistance ( $\Omega$ ) or cell flow field channels hydraulic resistance (Pa s m<sup>-3</sup>)  
 $R_{cn}$  Cell  $n$  flow field channels hydraulic resistance (Pa s m<sup>-3</sup>)  
 $R_m$  Cell manifolds hydraulic resistance (Pa s m<sup>-3</sup>)  
 $R_{mn}$  Cell  $n$  manifolds hydraulic resistance (Pa s m<sup>-3</sup>)  
 $R_n$  Cell  $n$  total hydraulic resistance (Pa s m<sup>-3</sup>)  
 $R_{\text{ohm}}$  Membrane resistance ( $\Omega$ )  
 $R_{\text{ohm,b}}$  Membrane resistance during the pre-contamination phase ( $\Omega$ )  
 $R_{\text{ohm,c}}$  Membrane resistance during the contamination phase ( $\Omega$ )

$R_W$	Cathode generalized finite length Warburg element resistance ( $\Omega$ )
$T_a$	Ambient temperature (K)
$T_{\text{cell}}$	Cell temperature (K)
$T_{\text{c,in}}$	Inlet coolant temperature (K)
$T_{\text{c,out}}$	Outlet coolant temperature (K)
$T_s$	End plate surface temperature (K)
$t_W$	Cathode generalized finite length Warburg element time constant (s)
$V_b$	Cell voltage during the pre-contamination phase used as baseline value (V)
$V_c$	Cell voltage during the contamination phase (V)
$V_r$	Cell voltage during the recovery phase (V)
$V_s$	Stack voltage (V)
$V_{\text{tn}}$	Thermo-neutral cell voltage (V)
$W_{\text{sc}}$	Cathode generalized finite length Warburg element
$Z_{\text{CPE}}$	Cathode constant phase element impedance ( $\Omega$ )
$Z_W$	Cathode generalized finite length Warburg element impedance ( $\Omega$ )
$\alpha_{\text{CPE}}$	Cathode constant phase element exponent
$\alpha_W$	Cathode generalized finite length Warburg element exponent
$\Delta T$	Coolant temperature rise between stack inlet and outlet (K)
$\Delta V_{\text{end}}$	Voltage difference between an end cell and the stack inner cells linear regression (mV)
$\omega$	Angular frequency ( $\text{rad s}^{-1}$ )

## 1 Introduction

PEMFCs have gained a noteworthy place among alternative power systems owing to favorable figures of merit and environmental benefits [1]. However, efforts are still needed to reduce cost and increase performance and durability to ensure commercial competitiveness. Fuel cells are expected to be exposed to many air contaminants [2]. The air filter is designed to minimize contaminant concentration but its scrubbing efficiency is less than 100 % and it has a limited life [3]. Most contamination studies were completed with single cells. As a result, relatively little is known about the impact of contaminants on the operational behavior of a stack [4]. It is surmised that an uneven cell performance change distribution will develop because operating conditions are uneven within a stack [5]. For example, the finite manifold size leads to unequal reactant flows between cells [6]. End cells in close contact with heat conductive end plates are cooler [7–9]. These statements are supported by the observation that temperature, contaminant concentration as well as dosage (the product of concentration, flow rate, and exposure duration) significantly impact contamination

[10]. Furthermore, uneven current distribution measurements in the presence of CO also indicate that current density is dosage dependent (dosage varies as CO adsorbs and reacts along the flow field length) [11].

Only two contamination studies related to fuel cell stacks were found. The concentration of Pb and Zn in membrane/electrode assemblies after aging was observed to vary along the stack length [12]. The Pb and Zn distributions were explained by the liquid water distribution within the stack with more droplets and higher ionic contaminant dosages near the fuel cell inlet. The presence of cell performance variations in a 3-cell stack resulting from ethylene glycol contamination was reported but was not noted by the authors [13]. Three-cell stacks are also not representative of pre-commercial fuel cell systems which contain several ten up to a few hundred cells. Contamination mechanisms leading to an uneven cell performance distribution are also unclear for several contaminant classes including inorganic ( $\text{SO}_x$ ,  $\text{NO}_x$ , etc.) and organic contaminants.

A two-step down selection procedure was recently employed to identify the most relevant organic contaminants in air for PEMFCs [14]. Propene was selected as a model contaminant for the present study because (i) it is present in air at a concentration varying from 0.03 to 0.2 ppm [14] (35 million tons per year produced in North America and Europe mostly for the manufacture of polypropylene and as a feedstock for the petrochemical industry), (ii) it has a significant impact on cell performance, (iii) the performance loss is due to increases in both kinetic and other overpotentials, a situation similar to the other 6 down selected organic contaminants [15], and (iv) upon recovery from a temporary exposure, an unusual gain in performance has been observed [14, 16, 17]. It was deemed relevant to duplicate prior results to ascertain the supra-recovery observation. A fuel cell stack was contaminated with propene and its performance was characterized with individual cell voltage, temperature, and impedance spectroscopy measurements. Results were used to obtain and explain the uneven impact of propene on the cell voltage distribution. It is emphasized that the present study focuses on the impact of contamination on PEMFC cell performance distributions rather than the determination of contamination mechanisms at the local level (catalyst, membrane, etc.) because these latter analyses are already ongoing elsewhere [15, 17, 18].

## 2 Experimental

A proprietary Protonex 36-cell stack (G6-210-36) with an active area of  $\sim 21 \text{ cm}^2$  and active section length of  $\sim 11 \text{ cm}$  was used [19]. Cells are connected in electrical series whereas reactants and water coolant are fed in

parallel with externally molded manifolds and serpentine flow field channels. The external molded manifolds simplify manufacturing and decrease the number of parts leading to significant cost savings. The stack is also internally and fluidly connected using U-type manifolds with air and coolant inlets and outlets located on the same end plate. This stack configuration is preferred due to packaging ease and a better performance [6]. The membrane/electrode assembly materials are commercially available and include a Pt catalyst, a Nafion ionomer and membrane, and a carbon based gas diffusion layer treated with a hydrophobic agent for water management. These key stack features are sufficient to discuss the performance distribution of a stack subject to contamination. The stack was operated with a custom test station designed for hardware-in-the-loop measurements characterized by a dynamic response time  $\leq 0.1$  s [20, 21]. The specified stack supplier operating conditions are as follows: air/H<sub>2</sub>, 2.5 stoichiometry/dead end with intermittent purges, 75/0 % relative humidity, and ambient/ambient pressure outlets, 55 °C, 1 A cm<sup>-2</sup>. These baseline conditions were varied to obtain additional diagnostic information. The air stream relative humidity, coolant flow rate, and current density were selected within the following respective ranges: 50 to 100 %, 1 to 1.75 L min<sup>-1</sup>, and 0.2 to 1 A cm<sup>-2</sup> for a constant air flow rate corresponding to a 2.5 stoichiometry at 1 A cm<sup>-2</sup>. Additionally, the temperature distribution was locally modified by cooling one end of the stack with a fan. Propene was injected in the air stream for a fixed period after the stack reached a steady-state voltage and at a constant rate after the humidifier to minimize the scavenging effect of liquid water [22]. After the scheduled exposure to 50 ppm, the propene injection was stopped when the stack reached a steady-state voltage. The stack was then allowed to recover until a new steady-state voltage was attained. During the test, impedance spectra were periodically measured and recorded using a proprietary multi-channel device (0.5 A signal amplitude or  $\sim 2.3$  % of the total current, 0.5 Hz to 10 kHz). A shunt resistor added in series with one of the electronic load cable connected to the stack bus plate provides the current signal. Electrical connections are also added to each bus plates and bipolar plates to obtain single cell voltage signals. Impedance spectra were analyzed using ZView software from Scribner Associates (version 3.3d). Temperature measurements were also obtained using resistance temperature detectors to determine ambient, coolant inlet and outlet, and manifold end plate temperatures.

Other diagnostic techniques were not contemplated at this stage because they would have required extensive modifications of the proprietary stack design and the existence of stack effects was not initially confirmed. For example, reactant flow distribution measurements either

require the use of pressure transducers along the manifold length [23] or the inclusion of a hot-wire anemometer into the manifold [24]. As an additional example, cyclic voltammetry, which can be used to assess the extent of propene adsorption on Pt catalysts or the presence of propene side reactions [18], requires individual electrical connections to each cell [25]. The situation is even more complicated if simultaneous measurements for each single cell are desirable to minimize errors and data acquisition time.

## 3 Results and discussion

### 3.1 Data analysis and propene contamination mechanism

Figure 1a illustrates the average cell voltage evolution during a test. During the first phase, the stack has a steady-state output (0.641 V). In the subsequent phase, the propene is injected and the average cell performance immediately decreases. The average cell performance loss rate decreases until a steady state is reached (0.398 V). In the last phase, only air circulates and the average cell performance recovers at a rate which is greater than the decay rate observed during the second phase. The average cell performance recovery rate also decreases until a steady state is reached (0.647 V). The average cell performance after recovery is larger than the initial value by  $\sim 6$  mV. This transient behavior and larger average cell performance after recovery are consistent with prior single cell experiments [14, 16, 17].

Figure 1b depicts the cell voltage distribution  $V_b$  during the first phase (baseline) at 2 h (specific times are indicated in Fig. 1a by red dashed lines). The cell voltage distribution is relatively uniform with a linear regression indicating a 10.4 mV change between cells 1 and 36. The cell voltage distribution  $V_c$  (contamination) shows that propene contamination steepens and renders the distribution less uniform at the end cells, whereas the cell voltage distribution  $V_r$  (recovery) indicates that propene contamination has a positive effect and uniformly increases cell performance. These trends are better emphasized by displaying cell voltage differences  $V_b - V_c$  and  $V_r - V_b$  to isolate these contaminant effects and remove other causes of cell variability (Fig. 1c). Figure 1c shows these steady-state cell voltage change distributions obtained, respectively, at 3 h and 20 min and 7 h and 30 min by subtracting first phase data at 2 h. The cell voltage change distribution during contamination  $V_b - V_c$  is characterized by two main features. End cells have lower performance than their contiguous cells. The cell performance change for the other cells depicts an increasing value from cell 2 to cell 35 (0.57 mV cell<sup>-1</sup>). The cell voltage

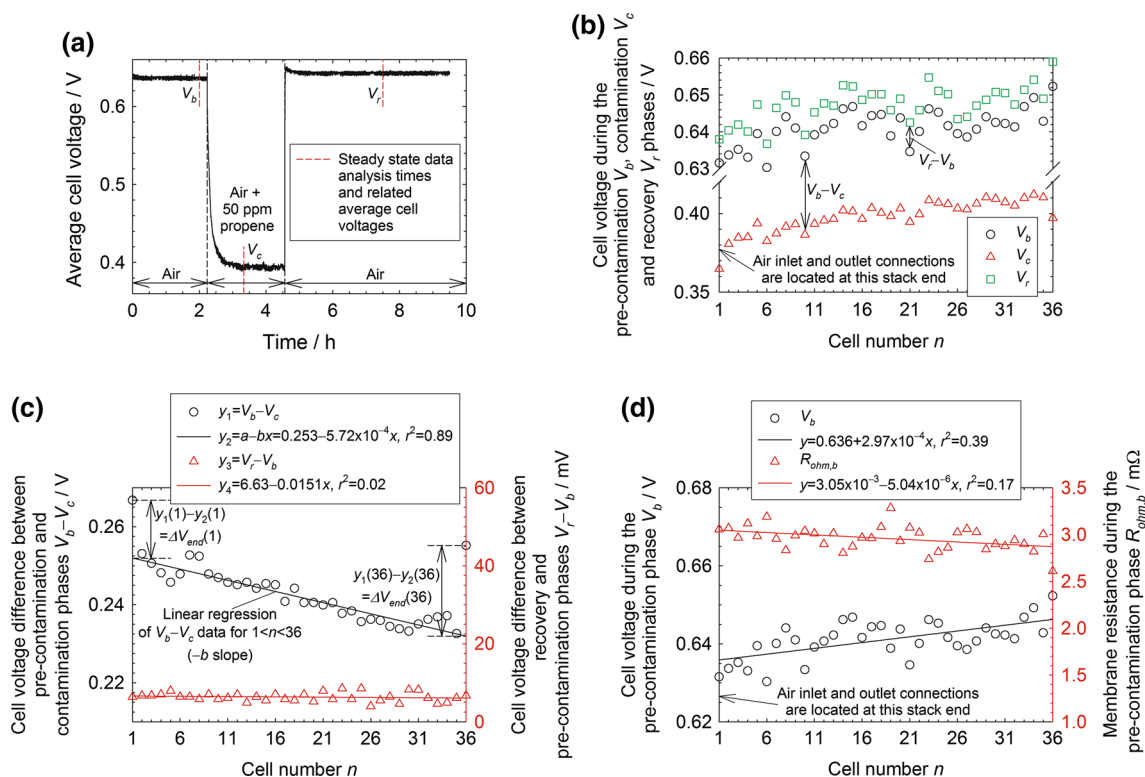


**Fig. 1** PEMFC stack average cell voltage before, during, and after a 50 ppm propene in air exposure (a). Individual cell voltages during the pre-contamination  $V_b$ , contamination  $V_c$ , and recovery phases  $V_r$  (b). Cell voltage differences between pre-contamination and

change distribution during recovery  $V_r - V_b$  is almost uniform and identical to the distribution observed before the contamination phase with the exception that cell voltages are higher by  $\sim 6$  mV on average. It is remarkable that such a small stack reveals clear effects during contamination (24 and 15 mV for respectively end cells 36 and 1, 19 mV along the stack core from cells 2 to 35). Contamination effects are expected to be even more significant in larger automotive or stationary stacks because it is relatively more difficult to control operating conditions over much larger volumes. In subsequent sections, two parameters derived from Fig. 1c data are used to discuss the effect of propene on stack performance. As end cells do not behave as inner cells, they are not taken into account to linearly correlate  $V_b - V_c$  data. The resulting slope  $-b$  is used as an indicator of the cell voltage distribution unevenness. The inner cells linear correlation is also used to calculate hypothetical voltage values for end cells 1 and 36 which are subsequently subtracted from corresponding measured values to define the voltage difference between end cells and inner cells  $\Delta V_{end}$ .

Figure 2a depicts the modified equivalent circuit which has been used to fit impedance spectra. A similar equivalent circuit was validated for  $\text{SO}_2$  contamination [26] but the inductance was not needed because very few high

contamination phases  $V_b - V_c$ , and recovery and pre-contamination phases  $V_r - V_b$  (c). PEMFC steady-state cell voltages  $V_b$  and membrane resistance  $R_{ohm,b}$  during the pre-contamination phase (d). Baseline operating conditions

frequency data points are characterized by positive imaginary impedance values (Fig. 2a). The equivalent circuit shown in Fig. 2a includes an ohmic resistor ( $R_{ohm}$ ) ascribed to the membrane and other resistive components such as contact resistances, an anode circuit ( $C_a, R_a$ ), and a cathode circuit (CPE $_c, R_c, W_{sc}$ ). The anode circuit is represented by a relatively small anode loop at high frequencies  $>1000$  Hz (Nyquist plot, Fig. 2b). The high frequency anode loop was also attributed to the frequency response of the shunt resistor used for measurements [27]. A correct anode loop assignment is however not relevant to the present discussion about the cathode contamination process. The cathode circuit leads to two loops [11, 26]. The mid-frequency range loop (Fig. 2b),  $<1000$  Hz and  $>10$  Hz, is ascribed to oxygen charge transfer and includes a constant phase element CPE $_c$  rather than a capacitor with impedance:

$$Z_{CPE} = 1/Q_{CPE}(j\omega)^{z_{CPE}} \quad (1)$$

The low frequency range loop (Fig. 2b),  $<10$  Hz, is ascribed to oxygen diffusion limitations in the cathode and is represented by a generalized finite length Warburg element  $W_{sc}$  with impedance:

$$Z_W = R_W \tanh[(j\omega t_W)^{z_W}] / (j\omega t_W)^{z_W} \quad (2)$$

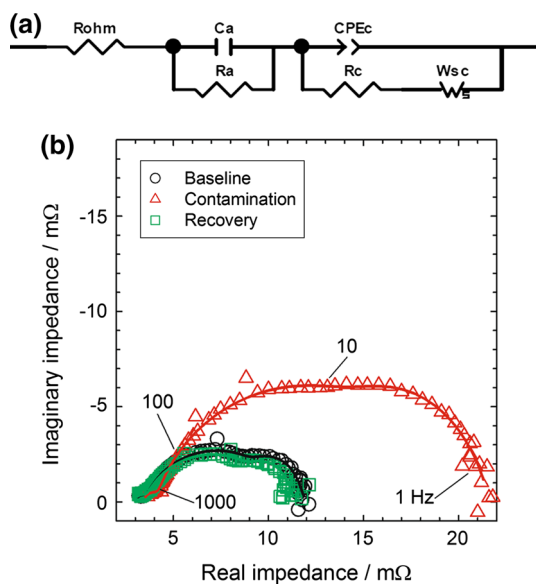


**Fig. 2** Equivalent circuit model for a PEMFC operated with air and contaminated air (a). Equivalent circuit model validation (line) with average PEMFC stack impedances (symbols) (b). Baseline operating conditions

Other equivalent circuits that include elements representing the presence of adsorbed intermediates on the cathode catalysts have also been described to take account of positive imaginary impedance values at low frequencies (the low frequency range loop is extended and includes an inductive behavior) [28–30]. Such positive imaginary impedance values are not observed during propene contamination. Figure 2b displays comparisons between the equivalent circuit model and average stack experimental data which are representative of individual cell data. Nyquist (Fig. 2b) as well as Bode representations (Online Resource 1 Figs. A1a and A1b) show good agreement. An adequate representation of the impedance data by the equivalent circuit is also observed for all single cells and all contamination stages under baseline conditions (data not shown). Table 1 lists all fitted equivalent circuit model parameters for all contamination stages (stack average). As a result of contamination, mid- and low frequency loops increase in size indicating an increase in kinetic and mass transfer resistances (Fig. 2b). After the recovery period, the same loops display a small decrease in size leading to smaller resistances and better cell performance (Figs. 1b and 2b). Several data points are scattered off the mid- and low frequency loops due to the short and intermittent hydrogen purges (Fig. 2b).

The equivalent circuit parameters (Table 1) provide additional information that clarifies the interaction between stack contamination and operating parameter distributions.

For instance, an attempt has been made to relate reactant flow to impedance spectroscopy data [31]. The observed cell voltage changes (Fig. 1c) represent overall values. Impedance spectroscopy resolves these changes into smaller and differentiated contributions (kinetic, ohmic, mass transfer). The small cell voltage changes of 24 and 15 mV for end cells, and 19 mV along the stack core (Fig. 1c), are resolved into 9 equivalent circuit parameters (Table 1). In general, parameter changes along the stack are relatively too small (standard deviations are the second entries in parentheses in Table 1) to show clear trends that can be distinguished from experimental uncertainties (parameter errors are the first entries in parentheses in Table 1) and cell variations due to manufacturing tolerances. Therefore, care should be exercised before drawing definitive conclusions. In the present case, only  $R_{ohm}$  and  $C_a$  parameter values' changes are substantially larger than their estimation errors. The  $R_{ohm}$  parameter is relevant to the present cathode contamination investigation and is discussed in Sect. 3.3.

The chemical and electrochemical behavior of propene provides the necessary background to derive the main features of a contamination mechanism. Propene adsorbs on carbon [32–34] and platinum [18, 35–39]. The presence of propene adsorbates on C affects the hydrophobicity of the gas diffusion layer, liquid water management, and the mass transfer resistance. It also affects mass transfer in the catalyst layer by lengthening the mass transfer path as the oxygen has to move around the region covered by the propene adsorbates to reach free Pt sites (decrease in real active area) [15]. The net effect based on Fick's first law is a decrease in reactant mass transfer rate leading to a larger mass transfer resistance. Finally, the propene adsorbates affect the oxygen reduction reaction because their presence limits the number of contiguous free Pt sites that favor the 2 electrons reduction pathway that leads to peroxide rather than water [15, 18, 40, 41]. Adsorbates on Pt are not limited to propene as oxidation and reduction (hydrogenation) reactions take place at potentials above 0.5 and below 0.2 V versus the standard hydrogen electrode (SHE) respectively [18, 42–44]. Propene residues left on C and Pt surfaces or induced changes to C and Pt surfaces are deemed responsible for the increased cell performance after the recovery phase (Figs. 1c and 2b, [17]). This mechanism is sufficient to discuss the present stack data and is consistent with cell voltage (Fig. 1a) and impedance (Fig. 2b) data (changes in kinetic and mass transfer resistances). Parallel studies are either completed or currently being completed using a variety of in situ (with a single cell) and ex situ methods to refine and further confirm the contamination mechanism [15, 17, 18].



**Table 1** Average equivalent circuit model parameter values at steady state for each contamination phase derived from Fig. 2b data

Parameter	Parameter value <sup>a</sup>		
	Before contamination	During contamination	During recovery
$R_{ohm}$ ( $\Omega$ )	0.0030 (0.000031/0.00013)	0.0035 (0.000032/0.00014)	0.0030 (0.000039/0.00013)
$C_a$ (F)	0.069 (0.010/0.038)	0.072 (0.0084/0.035)	0.058 (0.0096/0.034)
$R_a$ ( $\Omega$ )	0.00046 ( $3.1 \times 10^{-5}/3.4 \times 10^{-5}$ )	0.00065 <sup>b</sup> ( $3.7 \times 10^{-5}/3.0 \times 10^{-5}$ )	0.00051 ( $3.8 \times 10^{-5}/3.6 \times 10^{-5}$ )
$Q_{CPE}$ ( $s^{z_{CPE}} \Omega^{-1}$ )	2.2 (0.19/0.22)	1.5 <sup>b</sup> (0.12/0.10)	2.3 (0.24/0.22)
$\alpha_{CPE}$	0.80 (0.014/0.016)	0.84 (0.013/0.014)	0.78 (0.017/0.020)
$R_c$ ( $\Omega$ )	0.0073 (0.00025/0.00027)	0.015 <sup>b</sup> (0.00066/0.00047)	0.0069 (0.00027/0.00025)
$R_W$ ( $\Omega$ )	0.0012 (0.00021/0.00036)	0.0022 <sup>b</sup> (0.00058/0.00051)	0.0011 (0.00022/0.00036)
$t_W$ (s)	0.053 (0.0032/0.0061)	0.057 (0.0044/0.0048)	0.055 (0.0040/0.0069)
$\alpha_W$	0.70 (0.041/0.024)	0.70 (0.057/0.026)	0.70 (0.050/0.029)

<sup>a</sup> The parameter error and the standard deviation for the 36 single cell parameter values are in parentheses  
<sup>b</sup> The parameter value changed by more than 30 % during the contamination process

### 3.2 End cells effect

Individual cells in a stack are not subjected to the same operating conditions owing to design limitations [5]. The discussion is limited to end cells and inner cells effects which are both exacerbated during propene contamination (Fig. 1c). The end cells effect is discussed in this section, whereas the inner cells effect will be discussed in Sect. 3.3.

As a prelude, an analysis of the stack heat transfer is presented to facilitate the understanding of experimental observations and variables derived from experimental measurements. Figure 3a schematically shows natural convection heat losses. For inner stack cells 2 to  $n-1$ , the steady-state heat balance includes forced convection (all cells are equal and bounded by coolant flow fields on either side) and natural convection terms:

$$Q_{inner} = \dot{m}C\Delta T + Q_{sides} = \dot{m}C\Delta T + kA_{sides}(T_{cell} - T_a) \tag{3}$$

The natural convection term  $Q_{sides}$  corresponds to the heat loss from the cell sides. For end cells 1 and  $n$ , the steady-state heat balance is

$$Q_{1 \text{ or } n} = \dot{m}C\Delta T + Q_{sides} + Q_{end} = \dot{m}C\Delta T + k(A_{sides} + A_{end})(T_{cell} - T_a) \tag{4}$$

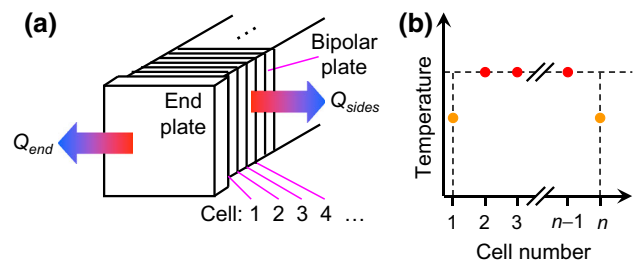


**Fig. 3** PEMFC stack heat losses (a) and schematic temperature distribution (b)

and includes an additional term  $Q_{end}$  for the natural convection heat loss from the end plate adjacent to the end cell. Equations (3) and (4) lead to

$$Q_{1 \text{ or } n} = Q_{inner} + kA_{end}(T_{cell} - T_a) > Q_{inner} \text{ for } T_{cell} > T_a \tag{5}$$

Therefore, end cells are cooler than inner cells because end cells have a greater heat loss (Fig. 3b). This effect has been recognized and exploited by either taking advantage of the situation or designing counter-measures to diminish cell non-uniformities [45–48]. The anomalous end cells behavior is consistent with a mathematical model that showed that a local heat anomaly such as an end cell only affects  $\sim 2$  adjacent cells with an impact progressively lessened with the distance from the anomaly [7]. In the

presence of propene contamination, the end cell effect is exacerbated as shown in Fig. 1c with the cell voltage difference between the pre-contamination and contamination phases  $\Delta V_{\text{end}}$ . After the contamination phase, the exacerbated end cell effect disappears as the cell voltage difference between pre-contamination and recovery phases is approximately constant for all cells (Fig. 1c). The exacerbated effect is ascribed to the lower local temperature [8, 9] and its significant effect on propene contamination [17]. The loss in cell performance for propene is approximately  $0.0086 \text{ \% } ^\circ\text{C}^{-1} \text{ ppm}^{-1}$  [17]. Therefore, the decrease in temperature is equal to 8.7 and 5.4 °C for an initial performance of 0.641 V (Fig. 1), end cell losses of, respectively, 24 and 15 mV (Fig. 1c), and a 50 ppm concentration ( $0.024$  or  $0.015 \text{ V} \times 100 / (0.641 \text{ V} \times 50 \text{ ppm} \times 0.0086 \text{ \% } ^\circ\text{C}^{-1} \text{ ppm}^{-1})$ ). The larger loss in cell performance at a lower temperature is mostly related to kinetic effects. Kinetic effects are represented by the oxygen reduction reaction [49, 50] and the contaminant oxidation reaction, which are both hampered by lower temperatures. Additionally, contaminant adsorption on the catalyst surface is favored at lower temperatures. Therefore, the oxygen reduction reaction proceeds more slowly at low temperature and is more impacted by the presence of the contaminant which is strongly adsorbed and is less easily removed by oxidation (for example,  $\text{SO}_2$  and  $\text{H}_2\text{S}$  oxidation [51, 52]). Mass transfer effects are not expected to play a significant role. Although, for example, the transport of oxygen [49] and contaminant ( $\text{H}_2\text{S}$ , for example, [53]) through the ionomer covering the catalyst is expected to be hampered at lower temperatures, the relatively low contaminant concentration (21 %  $\text{O}_2$  vs. 50 ppm propene) is not expected to hinder oxygen transport even if propene is a heavier molecule than  $\text{N}_2$ .

Equation (4) suggests that the end cell temperature can be changed by either varying the coolant flow rate (forced convection) or the ambient atmosphere air flow (natural convection). Heat removal is dependent on the coolant flow rate with a higher contribution from forced convection at higher coolant flow rates (Online Resource 1 Fig. A2). The heat produced by the fuel cell stack is calculated using

$$Q = I(nV_{\text{tn}} - V_s) \quad (6)$$

The forced convection heat loss is calculated using the first term on the right side of Eq. (3). The natural convection contribution is obtained by the difference between the heat generated and the forced convection heat removal. Both changes in coolant flow rate and ambient atmosphere air flow are employed to demonstrate the dependence of the end cell effect on the heat balance.

The last term on the right side of Eq. (4) corresponds to the end cell heat loss by natural convection. The heat transfer surfaces as well as the heat transfer coefficient

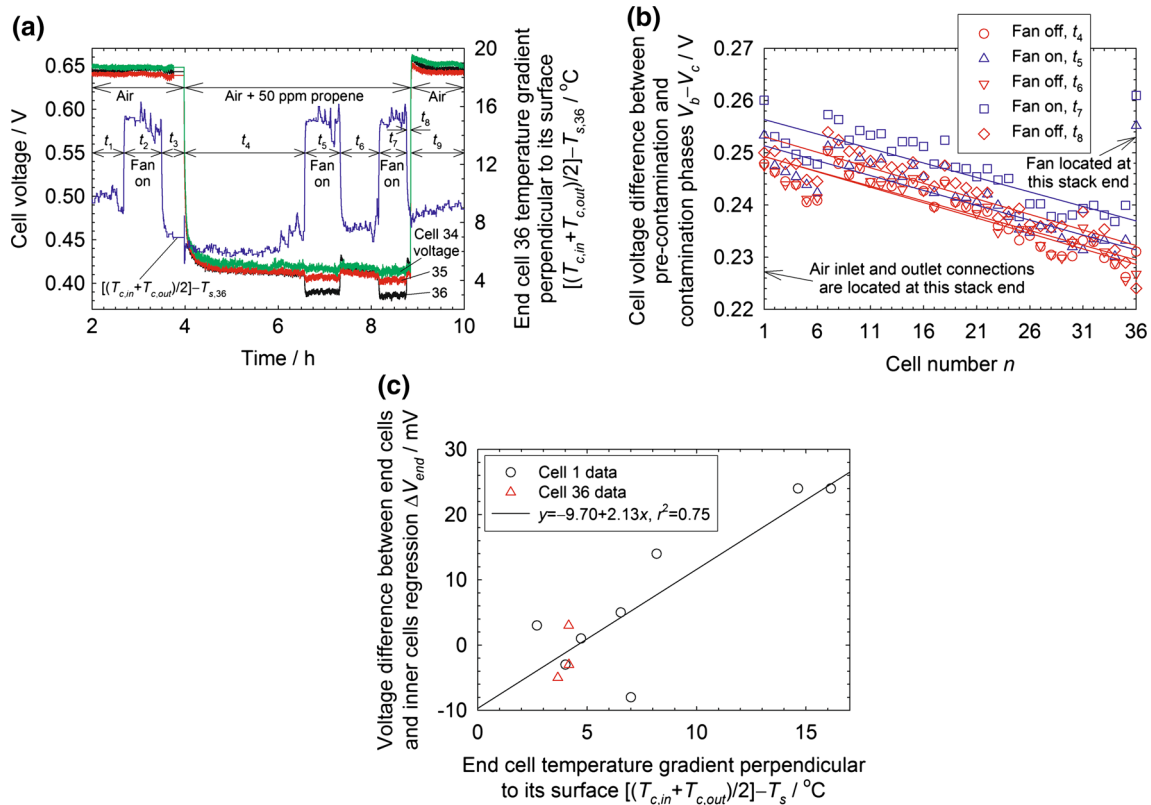
within the stack itself (conduction) are assumed to be constant because all experiments were carried out with the same stack. As a result, the natural convection heat loss is directly proportional to the temperature gradient  $T_{\text{cell}} - T_a$ . However, the individual cell temperatures are not accessible without stack design modifications. As a substitute, an approximate and more convenient temperature gradient is used and is formed by the difference between the average coolant temperature and the end plate surface temperature  $[(T_{\text{c.in}} + T_{\text{c.out}})/2] - T_s$ .

Figure 4a depicts the transient cell voltages for the last 3 cells of the stack (cells 34, 35 and 36). These cell voltage time series share the same features with the one illustrated in Fig. 1a. In addition, the calculated cell 36 approximate temperature gradient perpendicular to the cell plane is also included in Fig. 4a. The temperature gradient is intentionally modified by intermittently turning on and off a fan blowing air on the end plate adjacent to cell 36. The fan induces changes in the temperature gradient of  $\sim 7$  °C. The first change in temperature gradient takes place before the cell is contaminated by propene (period  $t_2$ ). This change negligibly affects all 3 cell voltages. By contrast, two additional temperature gradient changes during the contamination period ( $t_5$  and  $t_7$  periods) significantly affect end cell 36. The impact on cell 35 is relatively smaller, whereas cell 34 is hardly affected. Figure 4a data reveal that a link exists between the end cell performance during a contamination event and the end cell temperature.

Cell voltage distributions during time periods  $t_4$  to  $t_8$  are plotted in Fig. 4b. The inner cell distributions lie within a narrow band of approximately 8 mV in width indicating good data reproducibility. Also, the end cell 36 voltage is reversibly switched between 2 states by the action of the fan, a value close to the inner cells when the fan is off (red symbols) and a value significantly higher than inner cells (by  $\sim 18$  to 24 mV) when the fan is on (blue symbols). The differences between end and inner cells  $\Delta V_{\text{end}}$  are plotted in Fig. 4c against the temperature gradient. Other test data obtained under different coolant flow rates are also added to Fig. 4c, which show a strong correlation between end and inner cells voltage differences  $\Delta V_{\text{end}}$  and the temperature gradient confirming the hypothesis that the end cell performance is tied to its temperature during a contamination event.

### 3.3 Inner cells effect

Figure 5a schematically shows the reactant flow path for a U-type manifold [6], which is the preferred configuration for packaging purposes with all fluid ports located on the same stack end plate and for optimum performance. The corresponding flow resistance network is displayed in Fig. 5b. For cell 1, the total flow resistance, which includes stack manifolds and flow field channels contributions, is



**Fig. 4** PEMFC stack cells 34 to 36 voltage and end cell temperature gradient  $[(T_{c,in} + T_{c,out})/2] - T_s$  transients **(a)**. Cell voltage differences between pre-contamination and contamination phases  $V_b - V_c$  during different time periods **(b)**. Voltage difference between end

cells and inner cells regression  $\Delta V_{end}$  as a function of the end cell temperature gradient  $[(T_{c,in} + T_{c,out})/2] - T_s$  during contamination **(c)**. Intermittent operation of a fan directed toward cell 36. Otherwise baseline operating conditions for figures **a** and **b**

$$R_1 = R_{c1} + 2R_{m1} \tag{7}$$

For the other cells, the total flow resistance is

$$R_n = R_{cn} + 2 \sum_{i=1}^n R_{mi} \tag{8}$$

If all cells and manifold sections have the same resistance within manufacturing and design tolerances, Eqs. (7) and (8) reduce to

$$R_n = R_c + 2nR_m = R_1 + 2(n - 1)R_m > R_1 \text{ for } n \geq 2 \tag{9}$$

Equation (9) demonstrates that the reactant flow rate to each individual cell decreases along the stack length (Fig. 5c). In the presence of propene contamination, the flow distribution effect is also exacerbated as depicted in Fig. 1c with a gradual increase in cell voltage from cell 2 to cell 35 (stack inlet and outlet ports located at cell 1). As for the end cell effect, after the contamination phase, the exacerbated flow distribution effect disappears as the cell voltage difference between pre-contamination and

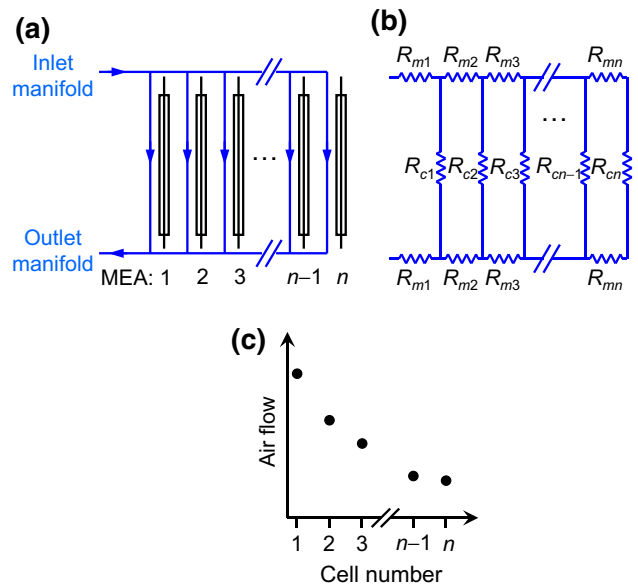


**Fig. 5** PEMFC stack air flow configuration (U-type manifold) **(a)**, equivalent flow resistance network **(b)**, and schematic air flow distribution **(c)**. MEA membrane/electrode assembly



recovery phases is approximately constant for all cells (Fig. 1c). The exacerbated effect is partly credited to the manifold and flow field channel flow resistances and resulting reactant and coolant flow distributions [5], leading to local variations in air flow, water management, and cell temperature, with the end cell 1 receiving a greater proportion of the sub-saturated stream that dehydrates the membrane and the coolant flow that controls the cell temperature to a set value. Evidence is provided by the membrane resistance distribution under baseline conditions  $R_{ohm,b}$  (Fig. 1d) with the end cell 1 having a larger resistance than the other cells (for  $R_{ohm}$ , the parameter error is much smaller than the standard deviation for the 36 single cell parameter values as indicated in Table 1). This dehydrating effect of the reactant flow has been incorporated into health diagnostic protocols [54]. Also, the distributed coolant flow leads to lower cell temperatures near the stack inlet and outlet connections which in turn create a larger propene effect and lower cell voltages (Fig. 1c) as discussed in Sect. 3.2.

The influence of water management on the propene effect and the inner cells performance distribution is also probed with variations in air relative humidity (Fig. 6a). Figure 6b demonstrates that a decrease in the inner cells regression slope  $-b$  accompanies an increase in the air relative humidity. This result is consistent with electrochemical propene oxidation which requires a water molecule and occurs at cathode potentials higher than 0.5 V versus SHE [43]. The cathode potential is estimated using a cell voltage of 0.398 V (Fig. 1a), an anode potential of 0 V versus SHE (hydrogen electrode), and an ohmic drop of 74 mV ( $1 \text{ A cm}^{-2} \times 21 \text{ cm}^2 \times 0.0035 \ \Omega$ , Fig. 1a and Table 1) yielding a cathode potential of 0.474 V versus SHE. Propene oxidation is favored by a larger relative humidity leading to a decrease of the catalyst coverage due to the formation of a weakly adsorbing  $\text{CO}_2$  product [55]. This is consistent with Fig. 6a results and a weaker propene effect for cells near cell 36, which experience wetter conditions and a lower membrane resistance (Fig. 1d). This

hypothesis is also consistent with literature reports linking contamination with reactant stream humidification [56, 57]. By contrast, the chemical oxidation of propene on the Pt catalyst which is not covered by the ionomer is inconsistent with the stack water management. Water inhibits the conversion of propene on Pt by oxidation [58, 59]. Therefore, for that specific case, propene should have a larger effect for cells near cell 36. The inner cells voltage regression slope is not equal to zero despite a locally invariant and saturated air relative humidity (Fig. 6b). Therefore, the stack water distribution is not the only factor responsible for the inhomogeneous inner cells voltage distribution.

The cell temperature distribution is important to explain the propene effect on the end cells performance. Consequently, the influence of the inner cells temperature distribution on the cell voltage distribution during propene contamination is investigated with variations in coolant flow rate (Fig. 7a and Online Resource 1 Fig. A2). The inner cells regression slope  $-b$  increases with the coolant flow rate (Fig. 7b). This observation is supported by model calculations with different fuel stoichiometries [60] and a progressively uneven flow distribution for higher flow rates. A simpler explanation is difficult to derive because the flow is complex and includes several effects that affect the flow regime such as flow development, directional changes, surface roughness (porous gas diffusion layer), and manifold/flow field channel differences. Figure 7b, however, clearly indicates that more than one factor influences the inner cells voltage distribution.

Additional data are obtained for several current densities while maintaining the air flow rate constant to minimally affect the flow distribution throughout the stack and facilitate result interpretation. Figure 8a reports the cell voltage difference distributions which are used to calculate the inner cells regression slope (Fig. 8b). Current densities are converted to a cathode potential using the steady-state cell voltage during contamination, an anode potential of 0 V versus SHE (hydrogen electrode), and the average stack ohmic resistance. As already mentioned, propene oxidizes

**Fig. 6** PEMFC stack cell voltage differences between pre-contamination and contamination (50 ppm propene in air) phases  $V_b - V_c$  as a function of the air inlet relative humidity (a). Inner cells linear regression slope during contamination as a function of the inlet air relative humidity (b). The solid lines are added as guides. Otherwise baseline operating conditions

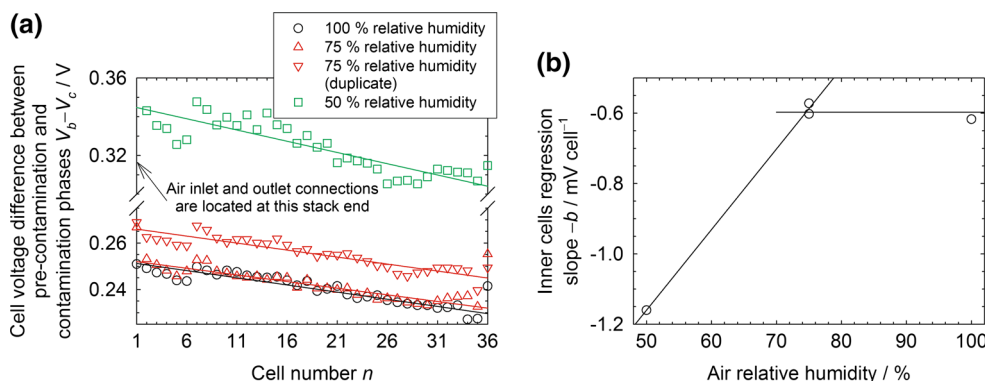


**Fig. 7** PEMFC stack cell voltage differences between pre-contamination and contamination (50 ppm propene in air) phases  $V_b - V_c$  as a function of the coolant flow rate (a). Inner cells linear regression slope during contamination as a function of the coolant flow rate (b). Otherwise baseline operating conditions

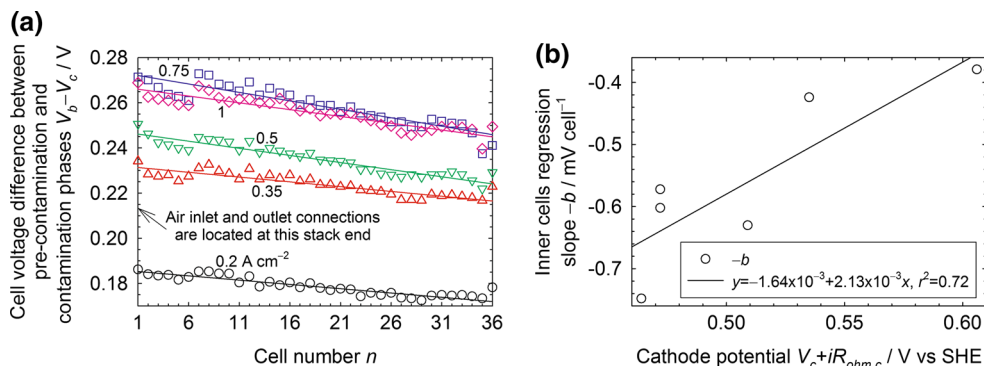
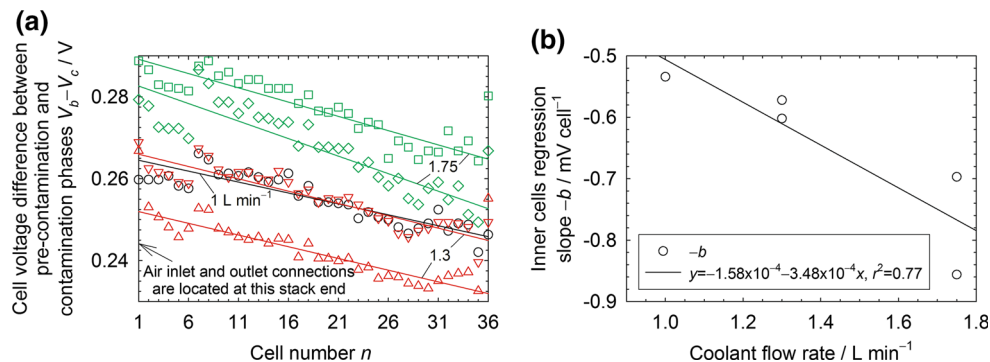


**Fig. 8** PEMFC stack cell voltage differences between pre-contamination and contamination (50 ppm propene in air) phases  $V_b - V_c$  as a function of the current density (a). Inner cells linear regression slope

to weakly adsorbing  $\text{CO}_2$  above a potential of 0.5 V versus SHE [43] which frees the catalyst surface and lessen the propene effect. This statement is consistent with Fig. 8b results and a smaller inner cells distribution slope at higher cathode potentials. Results are also consistent with chemical propene oxidation which only occurs on Pt-based catalysts to a small extent at low temperatures. The propene light-off temperature (50 % conversion) is  $>450^\circ\text{C}$  [61]. The propene conversion is also less than 10 % for temperatures lower than  $100^\circ\text{C}$  [62] and  $150^\circ\text{C}$  [63].

Other changes in local stack operating conditions are discounted to explain the propene effect because they are not expected to significantly affect contamination kinetics. Propene is sparsely soluble in liquid water ( $1.2 \times 10^{-4}$  to  $0.57 \times 10^{-4}$  mol fraction at 1 atm for respectively 20 to  $50^\circ\text{C}$  [64]), and therefore, a scavenging effect [14, 22] is not expected to be significant. The change in pressure along the air manifolds and flow field channels that may affect contaminant adsorption kinetics, which are dependent on the contaminant partial pressure, is also not expected to be significant. A pressure drop of  $<4.2$  kPa is specified by the supplier between the stack air inlet and outlet ( $\sim 4\%$  decrease in pressure). The change in pressure along the stack depends on the gas manifolds and flow field channels. Even if the last cell does not receive any flow

during contamination as a function of the cathode potential (b). Constant air flow rate corresponding to a 2.5 stoichiometry at  $1\text{ A cm}^{-2}$ . Otherwise baseline operating conditions

(0 kPa pressure drop) and the first cell reaches the pressure drop specification (4.2 kPa pressure drop), the maximum pressure difference between cells is at most of the order of 2 % ( $[(101 + 4.2 + 101)/2 - (101 + 101)/2]/101$ ). In more practical terms, the pressure difference between stack cells is expected to be much smaller than 2 % as the flow distribution is relatively uniform as supported by the cell performance distribution  $V_b$  (Fig. 1b).

## 4 Conclusion

The effects of a temporary PEMFC stack exposure to propene were investigated. Propene exacerbated the uneven cell performance distribution along the stack length. Propene effects were ascribed to interactions with cell temperature, air flow, and water vapor distributions. The exacerbated uneven cell voltage distribution during contamination (Fig. 1b) has important technological implications. An uneven cell voltage distribution may be used to detect the presence of a contamination event with a cell voltage monitoring system [65, 66]. Also, with the assumption that the control system does not immediately trigger a fuel cell system shutdown, single cells that are subjected to different operating conditions will not age at

the same rate. This statement means that the stack cell voltage distribution will become more uneven over time and will more easily trigger a fuel cell system shutdown. Such a conclusion is supported, for example, by long duration fuel cell experiments with different reactant humidification levels that led to dissimilar times to failure by membrane gas crossover [67]. Therefore, efforts should be devoted to the development of early detection and preventive measures to reduce contamination risks in a stack.

The effect of air stoichiometry on the cell voltage change distribution  $V_b - V_c$  is expected to further clarify contaminant effects on a fuel cell stack performance. However, such experiments are not trivial because for low stoichiometries, liquid water flooding is more prevalent whereas large stoichiometries are limited by high pressure drops leading to significant changes in pressure. Therefore, the practically accessible air flow rate range is limited and may not be sufficient to induce flow regime and air flow distribution changes needed to study the behavior of stack inner cells.

The stack contamination mechanisms developed for propene are readily applicable to other organic and more prevalent inorganic contaminants. From that standpoint, the selection of propene was, in retrospect, not critical and other contaminants could have equally been chosen to complete the present study. A larger contaminant effect on stack end cells is possible for the other 6 studied organic contaminants considering that for naphthalene, the loss in cell performance is  $0.51 \% \text{ } ^\circ\text{C}^{-1} \text{ ppm}^{-1}$  [17], which is much larger than for propene ( $0.0086 \% \text{ } ^\circ\text{C}^{-1} \text{ ppm}^{-1}$ ). The end cell effect is expected to be small for  $\text{SO}_2$  because temperature has a small impact on cell performance loss between 45 and 80 °C [68]. Predictions for  $\text{NO}_2$  or CO are currently not possible because cell performance loss data at different temperatures were not found. For sub-saturated reactant streams, a more moderate contaminant effect on stack inner cells is anticipated for species that do not involve water in oxidation or reduction reactions. Similar to propene,  $\text{SO}_2$  [69],  $\text{NO}_2$  [70], and CO [71] oxidation reactions include a water molecule, and therefore, a more uneven contaminant effect on stack inner cells is expected for a sub-saturated reactant stream. However, this statement is based on overall reactions. For instance, the elementary rate determining step for CO oxidation involves an adsorbed hydroxyl species [72], and therefore, the inner cells voltage distribution may not be impacted. A larger contaminant effect is also expected for electrode potentials located in a region where only species adsorption takes place due to the absence of active mechanisms cleansing the catalyst surface. This is the case for both  $\text{SO}_2$  [73] and  $\text{NO}_2$  [70] which lead to adsorbates on the Pt surface in the PEMFC operating range of 0.6–1 V versus SHE.

**Acknowledgments** The authors are grateful to the United States Office of Naval Research (award N00014-12-1-0496) and to the Hawaiian Electric Company for their ongoing support to the operations of the Hawaii Sustainable Energy Research Facility.

#### Compliance with ethical standards

**Conflict of interest** The authors declare that they have no conflict of interest.

#### References

- Curtin S, Gangi J (2014) 2013 fuel cell technologies market report. United States Department of Energy, Energy Efficiency and Renewable Energy
- St-Pierre J (2009) Air impurities. In: Büchi FN, Inaba M, Schmidt TJ (eds) Polymer electrolyte fuel cell durability. Springer, New York, pp 289–321
- Kennedy DM, Cahela DR, Zhu WH, Westrom KC, Nelms RM, Tatarchuk BJ (2007) Fuel cell cathode air filters: methodologies for design and optimization. *J Power Sour* 168:391–399. doi:10.1016/j.jpowsour.2007.03.020
- St-Pierre J, Angelo M, Bethune K, Ge J, Higgins S, Reshetenko T, Virji M, Zhai Y (2014) PEMFC contamination—fundamentals and outlook. *Electrochem Soc Trans* 61(23):1–14. doi:10.1149/06123.0001ecst
- St-Pierre J (2009) Overview performance and operational conditions. In: Garche J, Dyer C, Moseley P, Ogumi Z, Rand D, Scrosati B (eds) Encyclopedia of electrochemical power sources, vol 2. Elsevier, Amsterdam, pp 901–911
- Chang PAC, St-Pierre J, Stumper J, Wetton B (2006) Flow distribution in proton exchange membrane fuel cell stacks. *J Power Sour* 162:340–355. doi:10.1016/j.jpowsour.2006.06.081
- Promislow K, Wetton B (2005) A simple, mathematical model of thermal coupling in fuel cell stacks. *J Power Sour* 150:129–135. doi:10.1016/j.jpowsour.2005.02.032
- Chang P, Kim G-S, Promislow K, Wetton B (2007) Reduced dimensional computational models of polymer electrolyte membrane fuel cell stacks. *J Comput Phys* 223:797–821. doi:10.1016/j.jcp.2006.10.011
- Pei H, Liu Z, Zhang H, Yu Y, Tu Z, Wan Z, Liu W (2013) In situ measurement of temperature distribution in proton exchange membrane fuel cell I a hydrogen-air stack. *J Power Sources* 227:72–79. doi:10.1016/j.jpowsour.2012.11.027
- St-Pierre J, Zhai Y, Angelo M (2012) Quantitative ranking criteria for PEMFC contaminants. *Int J Hydrog Energy* 37:6784–6789. doi:10.1016/j.ijhydene.2012.01.029
- Reshetenko TV, Bethune K, Rocheleau R (2012) Spatial proton exchange membrane fuel cell performance under carbon monoxide poisoning at a low concentration using a segmented cell system. *J Power Sour* 218:412–423. doi:10.1016/j.jpowsour.2012.07.015
- Büchi FN (2009) Heterogeneous cell ageing in polymer electrolyte fuel cell stacks. In: Büchi FN, Inaba M, Schmidt TJ (eds) Polymer electrolyte fuel cell durability. Springer, New York, pp 431–439
- Jung JH, Kim SH, Hur SH, Joo SH, Choi WM, Kim J (2013) Polymer electrolyte membrane fuel cell performance degradation by coolant leakage and recovery. *J Power Sour* 226:320–328. doi:10.1016/j.jpowsour.2012.10.090
- St-Pierre J, Zhai Y, Angelo MS (2014) Effect of selected airborne contaminants on PEMFC performance. *J Electrochem Soc* 161:F280–F290. doi:10.1149/2.057403jes

15. St-Pierre J, Ge J, Zhai Y, Reshetyenko TV, Angelo M (2013) PEMFC cathode contamination mechanisms for several VOCs—acetonitrile, acetylene, bromomethane, iso-propanol, methyl methacrylate, naphthalene and propene. *Electrochem Soc Trans* 58(1):519–528. doi:10.1149/05801.0519ecst
16. St-Pierre J, Angelo MS, Zhai Y (2011) Focusing research by developing performance related selection criteria for PEMFC contaminants. *Electrochem Soc Trans* 41(1):279–286. doi:10.1149/1.3635561
17. Zhai Y, St-Pierre J, Angelo M (2012) The impact of operating conditions on the performance effect of selected airborne PEMFC contaminants. *Electrochem Soc Trans* 50(2):635–647. doi:10.1149/05002.0635ecst
18. Ge J, St-Pierre J, Zhai Y (2014) PEMFC cathode catalyst contamination evaluation with a RRDE—propene and naphthalene. *Electrochim Acta* 138:437–446. doi:10.1016/j.electacta.2014.06.147
19. Osenar P, Vitella T, Lauder N, Avis S, Ferreira D, Rezac R (2011) Insert-molded, externally-manifolded, sealed membrane based electrochemical cell stacks. United States Patent 7,914,947
20. Randolph G, Moore RM (2005) Test system design for hardware-in-loop evaluation of PEM fuel cells and auxiliaries. *J Power Sour* 158:392–396. doi:10.1016/j.jpowsour.2005.09.058
21. Moore RM, Hauer KH, Randolph G, Virji M (2006) Fuel cell hardware-in-loop. *J Power Sour* 162:302–308. doi:10.1016/j.jpowsour.2006.06.066
22. St-Pierre J, Wetton B, Zhai Y, Ge J (2014) Liquid water scavenging of PEMFC contaminants. *J Electrochem Soc* 161:E3357–E3364. doi:10.1149/2.0291409jes
23. Costamagna P, Arato E, Achenbach E, Reus U (1994) Fluid dynamic study of fuel-cell devices—simulation and experimental validation. *J Power Sour* 52:243–249. doi:10.1016/0378-7753(94)02014-0
24. Na Y, Suh J, Song I, Choi K-H, Choi H, Kim KB, Park J-Y (2011) Stable operation of air-blowing direct methanol fuel cell stacks through uniform oxidant supply by varying fluid flow fixtures and developing the flow sensor. *Int J Hydrog Energy* 36:9205–9215. doi:10.1016/j.ijhydene.2011.04.183
25. Wasterlain S, Candusso D, Harel F, Hissel D, François X (2011) Development of new test instruments and protocols for the diagnostic of fuel cell stacks. *J Power Sour* 196:5325–5333. doi:10.1016/j.jpowsour.2010.08.029
26. Zhai Y, Bethune K, Bender G, Rocheleau R (2012) Analysis of the SO<sub>2</sub> contamination effect on the oxygen reduction reaction in PEMFCs by electrochemical impedance spectroscopy. *J Electrochem Soc* 159:B524–B530. doi:10.1149/2.067205jes
27. Cimenti M, Tam M, Stumper J (2009) High frequency artifacts in electrochemical impedance spectroscopy measurements on PEM fuel cells. *Electrochem Solid-State Lett* 12:B131–B134. doi:10.1149/1.3162829
28. Seland F, Tunold R, Harrington DA (2006) Impedance study of methanol oxidation on platinum electrodes. *Electrochim Acta* 51:3827–3840. doi:10.1016/j.electacta.2005.10.050
29. Córdoba-Torres P, Keddani M, Nogueira RP (2009) On the intrinsic electrochemical nature of the inductance in EIS—a Monte Carlo simulation of the two-consecutive steps mechanism: the rough 3D case and the surface relaxation effect. *Electrochim Acta* 54:6779–6787. doi:10.1016/j.electacta.2009.06.084
30. Ghosh S, Raj CR (2010) Facile in situ synthesis of multiwall carbon nanotube supported flowerlike Pt nanostructures: an efficient electrocatalyst for fuel cell application. *J Phys Chem C* 114:10843–10849. doi:10.1021/jp100551e
31. O'Rourke J, Arcak M, Ramani M (2008) Estimating air flow rates in a fuel cell system using electrochemical impedance. In: ASME 2008 dynamic systems and control conference, paper DSCC2008-2172. ASME, New York, pp 497–503
32. Strano MS, Foley HC (2001) Synthesis and characterization of catalytic nanoporous carbon membranes. *AIChE J* 47:66–78. doi:10.1002/aic.690470110
33. Cruz FJAL, Esteves IAAC, Mota JPB (2010) Adsorption of light alkanes and alkenes onto single-walled carbon nanotube bundles: Langmuirian analysis and molecular simulations. *Colloids Surf A* 357:43–52. doi:10.1016/j.colsurfa.2009.09.002
34. Ye P, Fang Z, Su B, Xing H, Yang Y, Su Y, Ren Q (2010) Adsorption of propylene and ethylene on 15 activated carbons. *J Chem Eng Data* 55:5669–5672. doi:10.1021/je100601n
35. Zaera F, Chrysostomou D (2000) Propylene on Pt(111) I. Characterization of surface species by infra-red spectroscopy. *Surf Sci* 457:71–88. doi:10.1016/S0039-6028(00)00336-8
36. Janin E, Ringler S, Weissenrieder J, Åkermark T, Karlsson UO, Göthelid M, Nordlund D, Ogasawara H (2001) Adsorption and bonding of propene and 2-butenal on Pt(111). *Surf Sci* 482–485:83–89. doi:10.1016/S0039-6028(00)00999-7
37. Valcárcel A, Ricart JM, Clotet A, Markovits A, Minot C, Illas F (2002) Theoretical study of the structure of propene adsorbed on Pt(111). *Surf Sci* 519:250–258. doi:10.1016/S0039-6028(02)02220-3
38. Perger T, Kovács T, Turányi T, Treviño C (2005) Determination of the adsorption and desorption parameters for ethene and propene from measurements of the heterogeneous ignition temperature. *Combust Flame* 142:107–116. doi:10.1016/j.combustflame.2005.03.001
39. Nykänen L, Honkala K (2011) Density functional theory study on propane and propene adsorption on Pt(111) and PtSn alloy surfaces. *J Phys Chem C* 115:9578–9586. doi:10.1021/jp1121799
40. Garsany Y, Baturina OA, Swider-Lyons KE (2007) Impact of sulfur dioxide on the oxygen reduction reaction at Pt/Vulcan carbon electrocatalysts. *J Electrochem Soc* 154:B670–B675. doi:10.1149/1.2736648
41. Elezović NR, Gajić-Krstajić L, Radmilović V, Vračar L, Krstajić NV (2009) Effect of chemisorbed carbon monoxide on Pt/C electrode on the mechanism of the hydrogen oxidation reaction. *Electrochim Acta* 54:1375–1382. doi:10.1016/j.electacta.2008.08.067
42. Stickney JL, Soriaga MP, Hubbard AT, Anderson SE (1981) A survey of factors influencing the stability of organic functional-groups attached to platinum-electrodes. *J Electroanal Chem* 125:73–88. doi:10.1016/S0022-0728(81)80325-7
43. Bełtowska-Brzezinska M, Luczak T, Baltruschat H, Müller U (2003) Propene oxidation and hydrogenation on a porous platinum electrode in acidic solution. *J Phys Chem B* 107:4793–4800. doi:10.1021/jp021726f
44. Yang M-L, Zhu Y-A, Fan C, Sui Z-J, Chen D, Zhou X-G (2010) Density functional study of the chemisorption of C-1, C-2 and C-3 intermediates in propane dissociation on Pt(111). *J Mol Catal A* 321:42–49. doi:10.1016/j.molcata.2010.01.017
45. Reiser CA, Resnick G (2004) End-cell thermal distancing for fuel cell system. United States Patent 6,824,901
46. Houlberg SE (2007) Fuel cell stack with passive end cell heater. United States Patent 7,160,640
47. Arthur DA, Alp AB (2010) Fuel cell stack end cell control methodology. United States Patent 7,718,291
48. Alp AB, Arthur DA (2011) Fuel cell reliability improvement by using stack end plate temperature sensors. United States Patent 7,862,949
49. Parthasarathy A, Srinivasan S, Appleby AJ, Martin CR (1992) Temperature-dependence of the electrode-kinetics of oxygen reduction at the platinum Nafion® interface—a microelectrode investigation. *J Electrochem Soc* 139:2530–2537. doi:10.1149/1.2221258
50. Thompson EL, Jorne J, Gasteiger HA (2007) Oxygen reduction reaction kinetics in subfreezing PEM fuel cells. *J Electrochem Soc* 154:B783–B792. doi:10.1149/1.2742305



51. Abdullah AM, Saleh MM, Awad MI, Okajima T, Kitamura F, Ohsaka T (2010) Temperature effect on the recovery of SO<sub>2</sub>-poisoned GC/nano-Pt electrode towards oxygen reduction. *J Solid State Electrochem* 14:1727–1734. doi:10.1007/s10008-010-1023-y
52. Sethuraman VA, Weidner JW (2010) Analysis of sulfur poisoning on a PEM fuel cell electrode. *Electrochim Acta* 55:5683–5694. doi:10.1016/j.electacta.2010.05.004
53. Sethuraman VA, Khan S, Jur JS, Haug AT, Weidner JW (2009) Measuring oxygen, carbon monoxide and hydrogen sulfide diffusion coefficient and solubility in Nafion membranes. *Electrochim Acta* 54:6850–6860. doi:10.1016/j.electacta.2009.06.068
54. Fouquet N, Doulet C, Nouillant C, Dauphin-Tanguy G, Ould-Bouamama B (2006) Model based PEM fuel cell state-of-health monitoring via ac impedance measurements. *J Power Sour* 159:905–913. doi:10.1016/j.jpowsour.2005.11.035
55. Pan Y, Zhang JM, Guan WM, Zhang KH, Chen S (2011) Adsorption site preference of CO<sub>2</sub> on the Pt(100) surface by ab initio calculations. *J Phys Chem Solids* 72:1–4. doi:10.1016/j.jpics.2010.09.017
56. St-Pierre J, Wilkinson DP, Knights S, Bos ML (2000) Relationships between water management, contamination and lifetime degradation in PEMFC. *J New Mater Electrochem Syst* 3:99–106
57. Urdampilleta IG, Uribe FA, Rockward T, Brosha EL, Pivovar B, Garzon FH (2007) PEMFC poisoning with H<sub>2</sub>S: Dependence on operating conditions. *Electrochem Soc Trans* 11(1):831–842. doi:10.1149/1.2780996
58. Marécot P, Fakche A, Kellali B, Mabilon G, Prigent M, Barbier J (1994) Propane and propene oxidation over platinum and palladium on alumina—effects of chloride and water. *Appl Catal B* 3:283–294. doi:10.1016/0926-3373(94)00003-4
59. González-Velasco JR, Botas JA, González-Marcos JA, Gutiérrez-Ortiz MA (1997) Influence of water and hydrocarbon processed in feedstream on the three-way behaviour of platinum-alumina catalysts. *Appl Catal B* 12:61–79. doi:10.1016/S0926-3373(96)00058-6
60. McGarry M, Grega L (2005) Effects of inlet mass flow distribution and magnitude on reactant distribution for PEM fuel cells. *J Fuel Cell Sci Technol* 3:45–50. doi:10.1115/1.2134736
61. Avila MS, Vignatti CI, Apesteguía CR, Garetto TF (2014) Effect of support on the deep oxidation of propane and propylene on Pt-based catalysts. *Chem Eng J* 241:52–59. doi:10.1016/j.cej.2013.12.006
62. Benard S, Ousmane M, Retailliau L, Boreave A, Vernoux P, Giroir-Fendler A (2009) Catalytic removal of propene and toluene in air over noble metal catalyst. *Can J Civil Eng* 36:1935–1945. doi:10.1139/L09-135
63. Benard S, Baylet A, Vernoux P, Valverde JL, Giroir-Fendler A (2013) Kinetics of the propene oxidation over a Pt/alumina catalyst. *Catal Commun* 36:63–66. doi:10.1016/j.catcom.2013.03.001
64. Serra MCC, da Fonseca MMR, Calado JCG, Palavra AMF (1998) Solubility of propene in water and in a mineral medium for the cultivation of a Xanthobacter strain. *J Solut Chem* 27:455–461. doi:10.1023/A:1022604705859
65. Mulder G, De Ridder F, Coenen P, Weyen D, Martens A (2008) Evaluation of an on-site cell voltage monitor for fuel cell systems. *Int J Hydrogen Energy* 33:5728–5737. doi:10.1016/j.ijhydene.2008.07.017
66. Brunner D, Prasad AK, Advani SG, Peticolas BW (2010) A robust cell voltage monitoring system for analysis and diagnosis of fuel cell or battery systems. *J Power Sour* 195:8006–8012. doi:10.1016/j.jpowsour.2010.06.054
67. Knights SD, Colbow KM, St-Pierre J, Wilkinson DP (2004) Aging mechanisms and lifetime, PEMFC and DMFC. *J Power Sour* 127:127–134. doi:10.1016/j.jpowsour.2003.09.033
68. Zhai Y, Bender G, Bethune K, Rocheleau R (2014) Influence of cell temperature on sulfur dioxide contamination in proton exchange membrane fuel cells. *J Power Sour* 247:40–48. doi:10.1016/j.jpowsour.2013.08.054
69. Ramaker DE, Gatewood D, Korovina A, Garsany Y, Swider-Lyons KE (2010) Resolving sulfur oxidation and removal from Pt and Pt<sub>3</sub>Co electrocatalysts using in situ x-ray absorption spectroscopy. *J Phys Chem C* 114:11886–11897. doi:10.1021/jp101977g
70. St-Pierre J, Jia N, Rahmani R (2008) PEMFC contamination model: competitive adsorption demonstrated with NO<sub>2</sub>. *J Electrochem Soc* 155:B315–B320. doi:10.1149/1.2833301
71. Lee SJ, Mukerjee S, Ticianelli EA, McBreen J (1999) Electrocatalysis of CO tolerance in hydrogen oxidation reaction in PEM fuel cells. *Electrochim Acta* 44:3283–3293. doi:10.1016/S0013-4686(99)00052-3
72. Marković NM, Ross PN Jr (2002) Surface science studies of model fuel cell electrocatalysts. *Surf Sci Rep* 45:117–229. doi:10.1016/S0167-5729(01)00022-X
73. O'Brien JA, Hinkley JT, Donne SW, Lindquist S-E (2010) The electrochemical oxidation of aqueous sulfur dioxide: a critical review of work with respect to the hybrid sulfur cycle. *Electrochim Acta* 55:573–591. doi:10.1016/j.electacta.2009.09.067